

Nonlinear modeling and characterization of ultrasoft silicone elastomers

Asimanshu Das,¹ Kenneth S. Breuer,^{1, a)} and Varghese Mathai^{1, b)}
School of Engineering, Brown University, Providence, Rhode Island 02912, USA

(Dated: 15 May 2020)

We introduce a strain-energy based nonlinear hyper-elastic formulation to model the material properties of ultrasoft dielectric elastomers over a wide range of elastic properties, prestretch, and thicknesses. We build on the uniaxial Gent formulation, and under the conditions of equi-biaxial strain, derive an expression for the bulge deformation versus pressure. A circular bulge test methodology is developed to experimentally measure the mechanical response of the silicone membranes. The Gent model captures both neo-Hookean and strain-stiffening behaviors, and gives predictions which are in agreement with experimental measurements. Membranes with different thinner fractions are characterized over nearly one order of magnitude variation in shear modulus. Stiffer membranes are observed to harden at lower stretch ratios due to the increased fraction of polymer chains in them. The present approach offers a simple and cost-effective procedure for characterizing soft membranes under commonly encountered biaxial deformation conditions.

Soft elastomeric materials find applications in a variety of fields spanning from tissue engineering and soft robotics to targeted cell-culture and self-sensing devices. They form an essential ingredient in bio-inspired engineering today, owing to their resemblance to organic tissues, tunability of mechanical response, capacity for electrical actuation (dielectric), and stable and non-reactive properties¹⁻⁵. While there are numerous potential applications of highly compliant soft materials, an essential step in their effective usage is to quantify their elastic response over a range of strains. Material characterization studies have mostly focused on acrylic-based elastomers⁶⁻¹⁰, which display significant viscoelastic losses^{4,11}. In comparison, silicone-based dielectric elastomers have comparatively lower losses⁴, offer greater control of elasticity and are well-suited for in-house fabrication by combining a base mixture with a thinner component. They can attain very large strains before reaching yield point (hyperelasticity), with strain-stiffening occurring at large deformations¹²⁻¹⁴.

A number of hyper-elastic material models have been proposed in literature to model the non-linear response (stress vs. stretch-ratio) of soft materials. Among these, the Ogden¹⁵, Yeoh¹⁶ and Arruda-Boyce¹⁷ models all sufficiently capture the material behavior through complex multi-parameter fits. However, besides the shear modulus parameter, the remaining fitting constants bear uncertain physical significance. In comparison, the hyper-elastic Gent model¹⁸ offers a simpler two-parameter constitutive relation composed of a shear modulus, G , and a locking parameter, J_m . Importantly, J_m is representative of the strain-stiffening behavior, which can, in principle, be deduced from molecular considerations of the degree of polymer cross-linking^{19,20}. While the Gent formulation has a few inherent limitations due to its two parameter fitting²¹, it has been subject to several improvements in recent years^{22,23}.

Uniaxial tensile testing is the most widely used method for material characterization, owing to its simplicity and one-dimensional stretch condition. The testing is conducted in

a Universal Testing Machine (UTM) and requires careful preparation of a thin sample (dog-bone shaped) in order to avoid stress concentrations near the gripped region. For soft materials, these can be challenging as sliding near the grips and thinning due to clamping stresses can affect the quality of results^{24,25}. Furthermore, a number of assumptions are involved in translating the one-dimensional material response to commonly seen experimental conditions of plane or volumetric strains. A viable alternative is presented by the circular bulge method^{26,27}. Here, an applied differential pressure causes a thin material to enlarge under equi-biaxial stretch conditions. While traditionally employed for characterizing sheet metals and thin strips²⁸⁻³⁰, recently, it has begun to be considered for soft materials such as hydrogels and PDMS^{31,32}. The biaxial state of strain calls for a separate derivation of the stress vs. stretch-ratio relation.

In this Letter, we study the non-linear deformations of silicone elastomer membranes subjected to equi-biaxial state of stretch. A constitutive relation is derived based on a two-parameter hyper-elastic formulation (Gent¹⁸ model). We adopt a circular bulge test (CBT) methodology, with pressure control, to obtain the deformation vs. pressure of membranes with different prestretch and elastic moduli. The model's predictions are compared with experiments, and a series of validations are conducted. Following these, membranes with various thinner fractions are characterized, and their hyper-elastic parameters (shear modulus and locking parameter) are estimated.

The membranes were fabricated from a platinum-based addition-cure type silicone rubber (Dragon Skin FX Pro-Shore Hardness 2A, Smooth-On Inc., Macungie, PA). The base material was composed of two constituent components: Part A, a silicone hydride and Part B, a vinyl compound that acts as a catalyst. To this mixture, a thinner component (TC 5005-C, BJB Enterprises Inc., Tustin, California) was added to control the material properties of the cured elastomer (see supplemental material for details of the fabrication). The membranes thickness, h , was measured using a microscope stage (See supplemental material). Thicknesses ranged from 200 – 1000 μm , which is small compared to the lateral dimension, D , of the membrane disk ($h/D \leq 0.01$). Therefore, the bending stiffness is assumed to be negligible when com-

^{a)}Electronic mail: kenneth_breuer@brown.edu

^{b)}Electronic mail: varghese_mathai@brown.edu

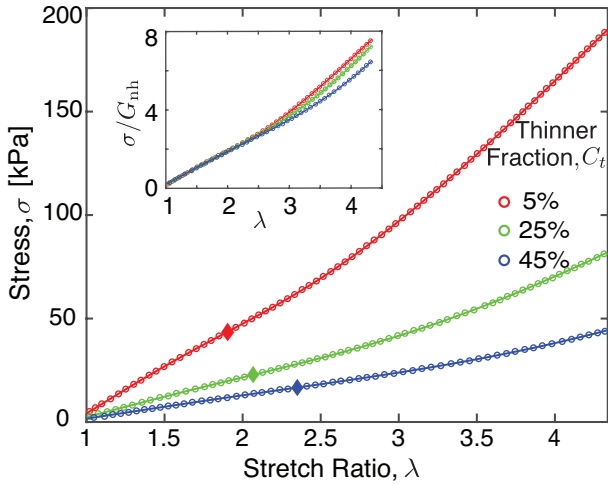


FIG. 1. Uniaxial stress vs. stretch-ratio data (circles) for silicone membrane samples with thinner fractions, $C_t = 5\%$, 25% and 50% . The solid curves show the Gent model fit to the data. The diamond symbols denote the respective onsets of strain stiffening in the samples, calculated from the inflection points of the respective curves. The inset presents stress divided by the best-fit neo-Hookean shear modulus, G_{nh} , which portrays clear evidence of the varying degree of strain-stiffening for the three cases.

pared to the tension in the membrane.

For uniaxial testing, dog-bone shaped samples were cut from membranes using a laser cutter and gripped between the jaws of a UTM (Instron 5942). Fig. 1 shows the stress vs. stretch-ratio curves for three representative cases with thinner fractions 5%, 25% and 50% by weight.

The curves do not follow a linear elastic behavior, and the material displays strain-stiffening for large values of λ , the onset of which is qualitatively marked by the diamond symbols in Fig. 1. The inset in the figure shows the same data normalized using a neo-Hookean fit: $\sigma = G_{nh}(\lambda - 1/\lambda^2)$, where G_{nh} are the respective shear moduli obtained using a least-squares fitting. For low stretch-ratios, the single-parameter neo-Hookean fit captures the material response well, while the model deviates significantly at large deformations. Interestingly, the point of departure from neo-Hookean behavior is a function of the thinner fraction, with the onset of strain-stiffening occurring at larger stretch-ratios for the softer materials.

To better describe the nonlinear behavior, we introduce the two-parameter Gent model¹⁸, which, for uniaxial stretch condition, is written as

$$\sigma = G_m \left(\lambda - \frac{1}{\lambda^2} \right). \quad (1)$$

Here, $G_m \equiv GJ_m/(J_m - I_1 + 3)$, where G is the shear modulus, J_m is the so-called “locking parameter” and I_1 is the first invariant of the left Cauchy-Green deformation gradient tensor³³. The Gent relation (Eq. 1) was fit to the uniaxial experimental data, which yielded the material constants, G and J_m . These constants will be used to evaluate the accuracy of the bulge test predictions.

For bulge testing, a circular cut-out (10 cm in diameter) was laser cut from a cured sheet of membrane and the membrane transferred onto a custom-built bi-axial stretching apparatus (see supplemental material Fig. S-3), which was used to achieve the desired pre-stretch, λ_0 . A circular acrylic ring of inner and outer diameters 120 mm and 127 mm, respectively, was glued onto the stretched membrane using a silicone adhesive (Silpoxy, Smooth-On Inc., Macungie, PA). Once the adhesive had cured (~ 60 mins), the membrane disk was mounted onto the bulge testing apparatus (Fig. 2a) using a rubber gasket to ensure that the chamber was air-tight.

A pressure regulator (Bellofram Type 70-Range 0-2 PSIG, Marsh Bellofram Corporation, Newell, WV), in combination with a bleed valve (Swagelok Stainless Steel Low Flow Metering Valve, Swagelok Company, Solon, OH), was used to establish the pressure in the test chamber, $p = p_{int} - p_{atm}$, which was monitored and recorded using a differential manometer (Reed R3001) with a resolution of 10^{-3} kPa. Images of the bulging membrane were recorded using a digital camera (Nikon D7200, 24.2 megapixel resolution), illuminated with a uniform back-light to ensure good image contrast (Fig. 2b). A checkerboard pattern, with a grid size of 10 mm, was used for calibration. The resolution of the image was 12 pixels/mm. The *Canny* edge detection algorithm was employed to extract the membrane shape (Fig. 2c). The apparatus was mounted on a rotating table so that images could be acquired from multiple positions in order to

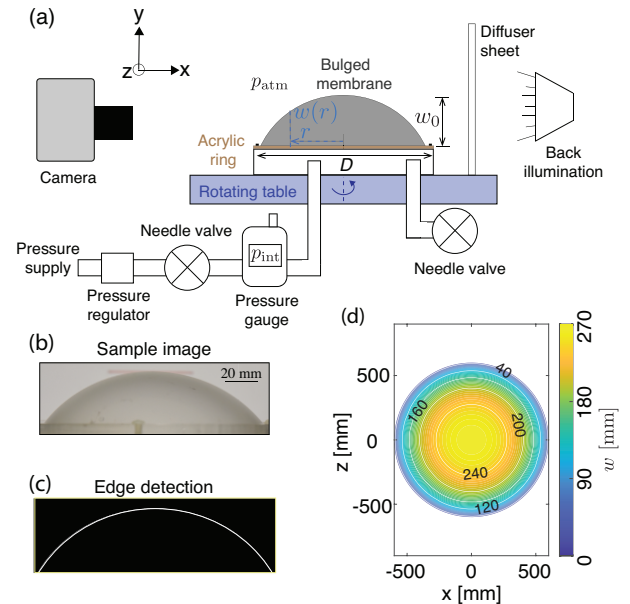


FIG. 2. Circular bulge testing procedures. (a) Schematic illustration of the bulge experimental setup. The needle valve regulates the pressure from the high-pressure supply. The bulge chamber is placed on top of a rotating table in order to capture the bulge from different angular orientations. (b) Sample image captured at an arbitrary deformation. (c) Edge detection on the sample image in (b). (d) Top view of the surface plot acquired by combining the deformation profiles from different angular views.

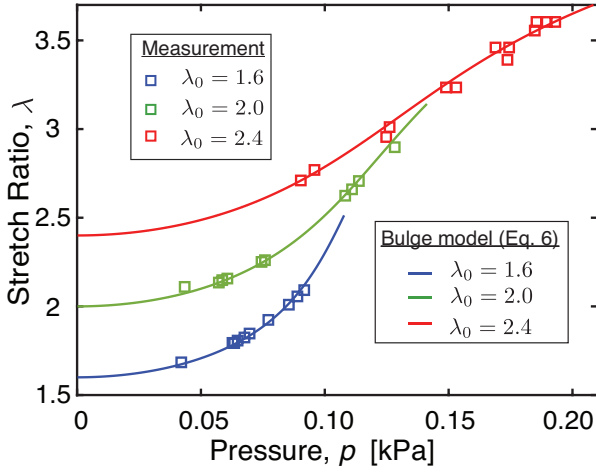


FIG. 3. Stretch-ratio vs. bulge pressure from experiments (square symbols) and the Gent biaxial model predictions (curves) for membranes with thinner fraction, $C_t = 25\%$, for three different pre-stretches, $\lambda_0 = 1.6, 2$ and 2.4 . In all of the three cases shown, the membrane deforms from a flat circular to a hemispherical shape, which corresponds to the stretch-ratio increase from λ_0 to $\frac{\pi}{2}\lambda_0$. The errorbars (estimated from three independent measurements) are smaller than the symbol size.

reconstruct the deformation of the entire membrane surface, $w(r, \theta)$, (Fig. 2d) and the centerline deformation, w_0 .

Data was taken over a range of pressures until the normalized bulge deformation, w_0/D , reached approximately 0.5. The membranes were observed to bulge nearly axisymmetrically (Fig. 2d), with $w(r)$ obeying a spherical cap deformation. Assuming a uniform applied pressure, p , and a spherical cap profile for the bulged membrane, the effective stretch-ratio in the deformed state can be approximated as³⁴

$$\lambda = \frac{2\lambda_0}{\kappa^*} \sin^{-1}(\kappa^*/2), \quad (2)$$

where $\kappa^* = \kappa D$ is the dimensionless curvature, and λ_0 is the pre-stretch ratio (see supplemental material for details).

The uniaxial Gent relation, used above, can be generalized to the axisymmetric bulge condition. During the bulge process, the membrane expands uniformly, and so the state of deformation can be approximated as equi-biaxial strain. Assuming an isotropic incompressible material, the deformation gradient tensor (\mathbf{F}) can be written as a diagonal matrix with elements: λ, λ , and $\frac{1}{\lambda^2}$. The Cauchy stress (σ_b) for incompressible Gent model can be written as

$$\sigma_b = -p\mathbf{I} + G_m\mathbf{B}, \quad (3)$$

where \mathbf{I} is the identity matrix and $\mathbf{B} = \mathbf{F}\mathbf{F}^T$ is the Cauchy-Green tensor. So the in-plane stresses are,

$$\sigma_{11} = \sigma_{22} = G_m(\lambda^2 - \frac{1}{\lambda^4}). \quad (4)$$

The resulting tension in the bulged membrane, T_b , is derived from the first Piola-Kirchhoff stress as $T_b = G_m h(1 -$

$1/\lambda^6)$. With the tension, T_b , in the bulged membrane known, the static equilibrium shape under uniform pressure loading can be obtained from the Young-Laplace equation³⁴,

$$\kappa + \frac{p}{T_b} = 0. \quad (5)$$

Substituting the constitutive relations (see supplemental material), we obtain a relation between the pressure and stretch ratio as

$$p \approx \frac{10G_m h}{D} (1 - \frac{1}{\lambda^6}) \sqrt{\lambda/\lambda_0 - 1} \quad (6)$$

Experimental measurements from the circular bulge test (CBT) of the stretch ratio vs. pressure are indicated by the square symbols in Fig. 3. The solid lines show the Gent model predictions (Eq. 6), where the constants, G and J_m , are determined from previously conducted uniaxial tests. Here, the blue, green and red curves correspond to three different pre-stretches, $\lambda_0 = 1.6, 2.0$ and 2.4 , respectively and all three show excellent agreement between measurements and theory. Interestingly, for the lowest value of pre-stretch, $\lambda_0 = 1.6$, the material response lies in the neo-Hookean regime, whereas strain-stiffening is noticeable for the highest pre-stretch case, $\lambda_0 = 2.4$. Similarly, the predictions match for independent variations in pre-stretch, λ_0 , and membrane thickness, h , (Fig. S-5, supplemental material). These validations establish the robustness of the two-parameter Gent formulation. Note that, at sufficiently large stretch-ratios, Eq. 6 reduces to $p \approx \frac{10G_m h}{D} \sqrt{\lambda/\lambda_0 - 1}$. For the largest stretch-ratio attained in the present work ($\lambda \approx 3.5$ in Fig. 3), this approximation is reasonable. The current model is applicable up to a maximum deformation, $w_0/D = 0.5$, or, equivalently, $\lambda/\lambda_0 \leq \pi/2$. Beyond this limit, the spherical cap assumption for the deformation is no longer valid.

Having demonstrated that the predictions of the Gent model are in good agreement with experimental measurements over a range of pressures, we now characterize the modulus, G , and the locking parameter, J_m , for membranes materials with varying thinner concentration, C_t (Fig. 4a, b). Overall, by varying C_t in the range: 0 – 50 %, the material's stiffness, G , can be modified by nearly an order of magnitude, which demonstrates the wide tunability in properties achievable with these ultra-soft silicone elastomers. Concurrently, the locking parameter, J_m , increases with C_t , indicating a delay in the onset of strain-stiffening. This can be explained by the reducing fraction of cross-linking polymers. Thus, with growing thinner concentration, the membrane behavior tends toward the simpler neo-Hookean solid³⁵, which is nicely captured in the Gent formulation.

In summary, we have introduced a circular bulge test methodology for estimating the hyper-elastic parameters of highly compliant membranes for a range of membrane elastic properties, pre-stretches and thicknesses. A two-parameter phenomenological model (Gent model¹⁸), based on the limiting chain extensibility, was adopted and extended theoretically for equi-biaxial condition to derive a relation between pressure and bulge deformation. The model was validated using independent measurements from uniaxial and circular

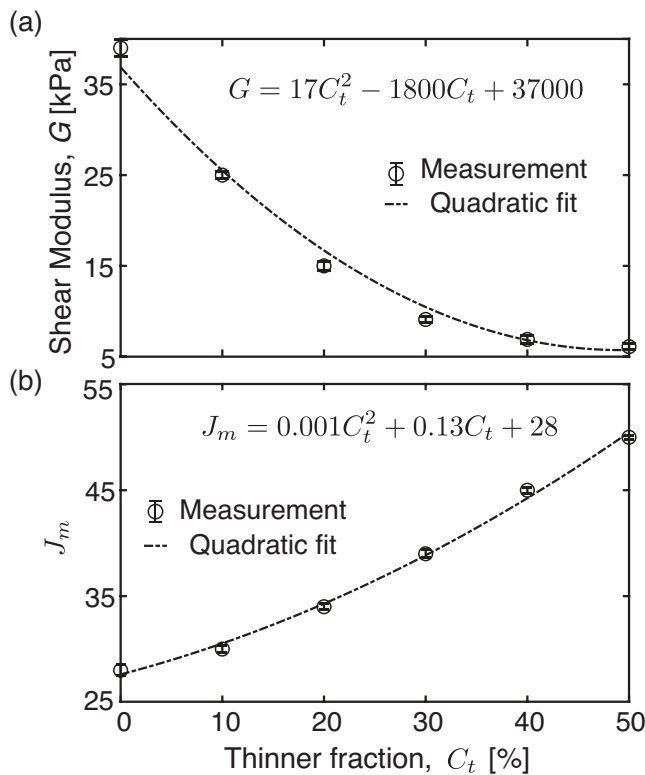


FIG. 4. Gent hyper-elastic constants obtained using the circular bulge testing methodology. (a) Shear modulus (G) for varying weight percentages of thinner, C_t . (b) Dependence of the locking parameter (J_m) on the thinner percentage. J_m is a representative of the onset of stiffening. Error bars represent maximum experimental variation from the mean. The polynomial fits in (a) and (b) provide useful relations to obtain the material properties for arbitrary choice of thinner percentage C_t .

bulge tests, and following this, a systematic characterization of the membrane properties with changing thinner concentration was performed. Both the shear modulus, G , and the locking parameter, J_m , exhibit a dependence on the amount of thinner added. Since the locking parameter quantifies the onset of strain-stiffening, the current model can, in principle, be applied to a wider class of soft polymers, including hydrogels, organic elastomers and soft dielectrics. The theoretical formulation introduced here can also be extended to anisotropic membranes and to non-equiaxial stretch conditions. The methods introduced here provide a reliable means to characterize ultra-soft membranes, which can replace expensive testing procedures requiring Universal Testing Machines.

Supplementary material

Supplementary material contains details of the biaxial modeling, the circular bulge test experiments, and videos of the stretching and unwrinkling procedure.

We thank Anupam Pandey, Pradeep Guduru and Jilian Bohnker for useful insights. This research was supported

by the US Army Natick Soldier Systems Center. The data that support the findings of this study are available from the corresponding author upon reasonable request.

- ¹H. Yuk, T. Zhang, G. A. Parada, X. Liu, and X. Zhao, "Skin-inspired hydrogel-elastomer hybrids with robust interfaces and functional microstructures," *Nat. Commun.* **7**, 12028 (2016).
- ²J. M. Stout, T. M. Welker, and A. R. Hawkins, "Electrostatically actuated membranes made from silica thin films," *Appl. Phys. Lett.* **110**, 053105 (2017).
- ³E. T. Roche, R. Wohlfarth, J. T. Overvelde, N. V. Vasilyev, F. A. Pigula, D. J. Mooney, K. Bertoldi, and C. J. Walsh, "A bioinspired soft actuated material," *Adv. Mater.* **26**, 1200–1206 (2014).
- ⁴J. Bohnker, *Sensing and Control of Flows over Membrane Wings*, Ph.D. thesis, Brown University (2019).
- ⁵A. Song, X. Tian, E. Israeli, R. Galvao, K. Bishop, S. Swartz, and K. Breuer, "Aeromechanics of membrane wings with implications for animal flight," *AIAA J.* **46**, 2096–2106 (2008).
- ⁶M. Wissler and E. Mazza, "Mechanical behavior of an acrylic elastomer used in dielectric elastomer actuators," *Sens. and Actuat. A: Phys.* **134**, 494–504 (2007).
- ⁷S. Michel, X. Q. Zhang, M. Wissler, C. Löwe, and G. Kovacs, "A comparison between silicone and acrylic elastomers as dielectric materials in electroactive polymer actuators," *Polym. Int.* **59**, 391–399 (2010).
- ⁸R. Sahu and K. Patra, "Characterisation of tensile behaviour of a dielectric elastomer at large deformation," *Journal of The Institution of Engineers (India): Series C* **95**, 207–212 (2014).
- ⁹N. C. Goulbourne, "A constitutive model of polyacrylate interpenetrating polymer networks for dielectric elastomers," *Int. J. Solid. Struct.* **48**, 1085–1091 (2011).
- ¹⁰J. Maláč, "Elastomers: Characterization of tensile behaviour at lower deformations," *Polym. Test.* **24**, 790–792 (2005).
- ¹¹R. Palakodeti and M. Kessler, "Influence of frequency and prestrain on the mechanical efficiency of dielectric electroactive polymer actuators," *Mater. Lett.* **60**, 3437–3440 (2006).
- ¹²E. Hajiesmaili and D. R. Clarke, "Reconfigurable shape-morphing dielectric elastomers using spatially varying electric fields," *Nat. Commun.* **10**, 183 (2019).
- ¹³L. Léger and C. Creton, "Adhesion mechanisms at soft polymer interfaces," *Phil. Trans. Royal Soc. A: Math. Phys. Eng. Sci.* **366**, 1425–1442 (2007).
- ¹⁴B. Rashid, M. Destrade, and M. D. Gilchrist, "Mechanical characterization of brain tissue in compression at dynamic strain rates," *J. Mech. Biomed. Mater.* **10**, 23–38 (2012).
- ¹⁵R. W. Ogden, "Large deformation isotropic elasticity—on the correlation of theory and experiment for incompressible rubberlike solids," *Proc. Royal Soc. London A. Math. Phys. Sci.* **326**, 565–584 (1972).
- ¹⁶O. H. Yeoh, "Some forms of the strain energy function for rubber," *Rubber Chem. Technol.* **66**, 754–771 (1993).
- ¹⁷E. M. Arruda and M. C. Boyce, "A three-dimensional constitutive model for the large stretch behavior of rubber elastic materials," *J. Mech. Phys. Solid.* **41**, 389–412 (1993).
- ¹⁸A. Gent, "A new constitutive relation for rubber," *Rubber Chem. Technol.* **69**, 59–61 (1996).
- ¹⁹D. Hao, D. Li, and Y. Liao, "Hyperelasticity, dynamic mechanical property, and rheology of addition-type silicone rubber (vpdms cured by pmhs)," *J. Appl. Polym. Sci.* **132** (2015).
- ²⁰T. Beda, "Modeling hyperelastic behavior of rubber: A novel invariant-based and a review of constitutive models," *J. Polym. Sci. B: Polym. Phys.* **45**, 1713–1732 (2007).
- ²¹E. Pucci and G. Saccomandi, "A note on the gent model for rubber-like materials," *Rubber chemistry and technology* **75**, 839–852 (2002).
- ²²M. Destrade, G. Saccomandi, and I. Sgura, "Methodical fitting for mathematical models of rubber-like materials," *Proceedings of the Royal Society A: Mathematical, Physical and Engineering Sciences* **473**, 20160811 (2017).
- ²³M. Destrade, M. Gilchrist, J. G. Murphy, B. Rashid, and G. Saccomandi, "Extreme softness of brain matter in simple shear," *International Journal of Non-Linear Mechanics* **75**, 54–58 (2015).

- ²⁴J.-S. Plante *et al.*, *Dielectric elastomer actuators for binary robotics and mechatronics*, Ph.D. thesis, Massachusetts Institute of Technology (2006).
- ²⁵M. Hossain, D. K. Vu, and P. Steinmann, “Experimental study and numerical modelling of vhb 4910 polymer,” *Comput. Mater. Sci.* **59**, 65–74 (2012).
- ²⁶M. K. Small and W. Nix, “Analysis of the accuracy of the bulge test in determining the mechanical properties of thin films,” *J. Mater. Res.* **7**, 1553–1563 (1992).
- ²⁷C. Huang, W. Lou, C. Tsai, T.-C. Wu, and H.-Y. Lin, “Mechanical properties of polymer thin film measured by the bulge test,” *Thin Solid Films* **515**, 7222–7226 (2007).
- ²⁸J. Vlassak and W. Nix, “A new bulge test technique for the determination of young’s modulus and poisson’s ratio of thin films,” *J. Mater. Res.* **7**, 3242–3249 (1992).
- ²⁹G. Gutscher, H.-C. Wu, G. Ngaile, and T. Altan, “Determination of flow stress for sheet metal forming using the viscous pressure bulge (vpb) test,” *J. Mater. Proc. Technol.* **146**, 1–7 (2004).
- ³⁰A. Ranta-Eskola, “Use of the hydraulic bulge test in biaxial tensile testing,” *Int. J. Mech. Sci.* **21**, 457–465 (1979).
- ³¹J.-Y. Sheng, L.-Y. Zhang, B. Li, G.-F. Wang, and X.-Q. Feng, “Bulge test method for measuring the hyperelastic parameters of soft membranes,” *Acta Mech* **228**, 4187–4197 (2017).
- ³²S. Raayai-Ardakani, Z. Chen, D. R. Earl, and T. Cohen, “Volume-controlled cavity expansion for probing of local elastic properties in soft materials,” *Soft Matter* **15**, 381–392 (2019).
- ³³A. F. Bower, *Applied mechanics of solids* (CRC press, 2009).
- ³⁴R. M. Waldman and K. S. Breuer, “Camber and aerodynamic performance of compliant membrane wings,” *J. Fluid. Struct.* **68**, 390–402 (2017).
- ³⁵C. O. Horgan, “The remarkable gent constitutive model for hyperelastic materials,” *Int. J. Non-lin. of Mech.* **68**, 9–16 (2015).

Supplemental Material

Nonlinear modeling and characterization of ultrasoft silicone elastomers

Asimanshu Das,¹ Kenneth S. Breuer,^{1, a)} and Varghese Mathai^{1, b)}
School of Engineering, Brown University, Providence, Rhode Island 02912, USA

(Dated: 15 May 2020)

S-I. MEMBRANE FABRICATION AND TESTING

The membranes were fabricated by curing a platinum-based addition-cure type silicone rubber (Dragon Skin FX Pro-Shore Hardness 2A, Smooth-On Inc., Macungie, PA). The product consists of two parts: Part A, a silicone hydride and part B, a vinyl compound that acts as a catalyst. To this mixture, a thinner component (TC 5005-C, BJB Enterprises Inc., Tustin, California) was added to control the material properties of the cured rubber. The three components were mixed together and poured onto a flat polyethylene terephthalate (PET) film of dimensions 200 mm \times 300 mm and thickness 125 μ m. The PET film was placed on a leveled steel plate (CNC milled with 1 μ m surface roughness). A uniform wet-film thickness was obtained using a height-adjustable film applicator (TQC-SH0342-300, TQC Sheen B.V, LL Capelle aan den IJssel, Netherlands), with a least count of 10 micron. As the membrane mixture has a low viscosity, it flows and equilibrates in thickness inside a dam-like structure.

S-I-a. Membrane thickness characterization

The fabricated membranes were extremely thin and compliant. A non-intrusive method, comprising a video microscope and a 3-axis stage, was employed. The height of the stage was precisely controlled with a micrometer positioning system (positioning accuracy up to 1 μ m), that provided a robust method to not only measure thickness at a point, but also scan the entire surface to quantify for the variation in thickness. Here, the z-axis is the vertical movement of the stage. Talcum powder particles ($\sim 10 \mu$ m particles) were sprayed to ensure better identification of the top and bottom surfaces, as shown by the darkened spots in Fig. S-1b, c. The membranes, upon drying, became thinner than the original wet-films. The dry-film thicknesses of the fabricated membranes lies in the range: 300 μ m to 1500 μ m, with a thickness precision of $\pm 50 \mu$ m. For any chosen membrane, the thickness non-uniformity along the surface was $\pm 7.5 \mu$ m.

S-I-b. Membrane release

Because the membranes are very thin and soft, they are difficult to handle, and tend to fold and wrinkle in the presence

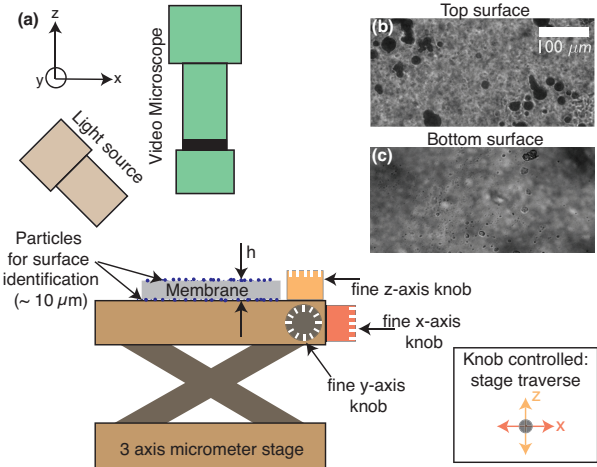


FIG. S-1. (a) Schematic of the thickness measurement setup. The stage facilitates 3-axis movement with its micrometer positioning system (positioning accuracy of 1 μ m). Here, the z-axis knob controls the vertical movement of the stage. Talcum powder particles are sprayed to ensure better identification of the top and bottom surfaces. (b) & (c) show images of the top and bottom surfaces of the membrane, respectively. The darkened spots are the talcum powder particles.

of residual electrostatic charges (due to peeling from the PET film). To unwrinkle the membrane, we suspended them in a water bath (as shown in Fig. S-2a). Since the membranes were nearly neutrally buoyant, this established a state where they could relax to their true shape. Fig. S-2b shows the unwrinkling of the membrane to its free state when it had low residual stresses (see also supplemental video S1). Note that immersion in the bath did not lead to any noticeable water absorption.

S-I-c. Uniaxial testing

Once cured, a “dog-bone” shape measuring 38 mm gauge length and 12 mm width was cut out from the cured membrane film using a laser cutter. The dog-bone sample was necessary to ensure a nearly uniaxial tensile load on the membrane. The sample was mounted onto two pairs of metal plates using adhesive tape (4910 VHB, 3M Company, Saint Paul, MN) and the specimen was gripped between the jaws of a Universal Testing Machine (Instron 5942). Load tests were carried out at a strain rate, $\dot{\epsilon}$, of 0.08 mm/s. This strain rate was chosen after carrying out tests at several values of $\dot{\epsilon}$ between 0.04 mm/s and 5 mm/s. Notably, the stress-strain curves showed little

^{a)}Electronic mail: kenneth_breuer@brown.edu

^{b)}Electronic mail: varghese_mathai@brown.edu

dependence ($\pm 2\%$) on the strain rate, $\dot{\epsilon}$.

S-I-d. Sample preparation for Biaxial stretching

In order to provide an initial pre-stretch to the membrane, a biaxial stretcher was designed, fabricated and used (Fig. S-3). The stretcher was designed in a way that rotation of the outer ring produced radial motion to the fingers holding the membrane sample. The stretcher is made from acrylic, and is composed of three main parts: (i) a base plate, (ii) a rotating frame and (iii) eighteen sliding fingers. The base plate houses the finger assembly and supports the rotating frame. The fingers distribute the stretching forces and ensure nearly equi-biaxial stretching. A representative example of the stretching operation is shown in supplemental video S2. The stretcher has a minimum diameter of 70 mm, and can stretch up to 240 mm, which gives a wide range of pre-stretches $\lambda_0 \in [1.0, 3.4]$. The part files provided as supplemental material can be used to reproduce the design.

S-II. THEORETICAL MODELING

The uniaxial stress (σ) for the Gent hyper-elastic model can be written as¹,

$$\sigma = G_m \left(\lambda - \frac{1}{\lambda^2} \right), \quad (\text{S-1})$$

where $G_m = \left(\frac{GJ_m}{J_m - I_1 + 3} \right)$, G is the shear modulus, J_m is the "locking parameter", and I_1 is the first invariant of the left Cauchy-Green deformation gradient tensor. The principal stretches for uniaxial extension are represented by λ_1, λ_2 and, λ_3 . Here $\lambda_1 = \lambda$ and $\lambda_2 = \lambda_3$. Assuming the material to be

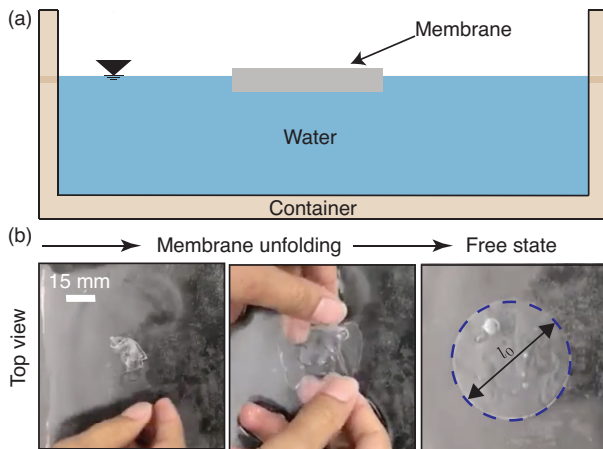


FIG. S-2. (a) Depicts a floating membrane on a water bath immediately after release from the PET film. (b) It shows the procedure of unwrinkling the membrane. The circular membrane has relaxed to its initial diameter (right side image), denoted by l_0 .

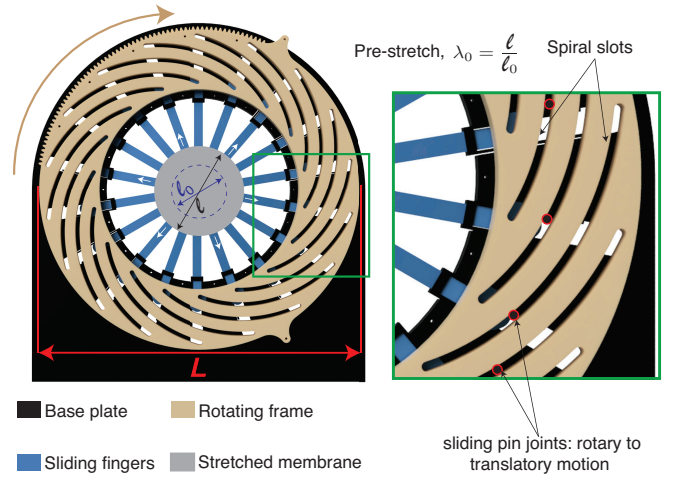


FIG. S-3. Schematic of the top view of biaxial stretching apparatus. The sliding pin joints trace the spiral profile, effectively converting the rotary motion into radial motion of the sliding fingers. This enables a nearly equi-biaxial stretching.

incompressible, $\lambda_1 \lambda_2 \lambda_3 = 1$. Consequently, the first invariant, $I_1 = \lambda_1^2 + \lambda_2^2 + \lambda_3^2$, reduces to $\lambda^2 + \frac{2}{\lambda}$.

In the bulge test, an initially flat circular membrane with a diameter, D , evolves into a nearly hemispherical shape when subjected to uniform pressure, p . We assume an incompressible hyper-elastic material with thickness, h , and pre-stretch, λ_0 . Assuming a spherical cap profile, we can express the curvature, κ , of the membrane as,

$$\kappa = \frac{8w_0}{D^2 + 4w_0^2}, \quad (\text{S-2})$$

where w_0 is the maximum deformation at the centre.

An illustration of the deformed segment is given by Fig. S-4. Based on simple geometrical considerations, we can express $\sin \theta = \frac{D}{2R}$ where 2θ is the angle of the deformed circular segment. Consequently, $\theta = \sin^{-1}(\kappa^*/2)$. The effective stretch-ratio in this deformed state can then be written as $\lambda = \lambda_0 \frac{2\theta R}{D}$, where λ_0 is the initial pre-stretch applied. Substituting this, we obtain:

$$\lambda = \frac{2\lambda_0}{\kappa^*} \sin^{-1}(\kappa^*/2), \quad (\text{S-3})$$

where $\kappa^* = \kappa D$. Expanding the inverse sine for small values of κ^* , and retaining terms to $\mathcal{O}(\kappa^{*3})$, we get

$$\sin^{-1}(\kappa^*/2) \approx \kappa^*/2 + \kappa^{*3}/48$$

and substituting this in Eq. S-3, the curvature can be written as

$$\kappa^* \approx 5\sqrt{\lambda/\lambda_0 - 1}. \quad (\text{S-4})$$

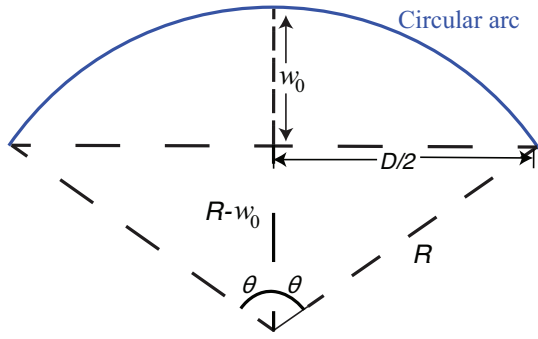


FIG. S-4. Schematic of the cross-sectional view of the membrane deformation.

Next, we extend the uniaxial Gent relation to equi-biaxial stretch condition. Assuming incompressibility of the material, the deformation gradient tensor (\mathbf{F}) for equi-biaxial extension can be written as a diagonal matrix with elements: λ, λ , and $\frac{1}{\lambda^2}$ respectively. The left Cauchy-Green tensor,

$$\mathbf{B} = \mathbf{F} \cdot \mathbf{F}^T. \quad (\text{S-5})$$

The Cauchy stress (σ_b) for incompressible Gent model can be written as,

$$\sigma_b = -p\mathbf{I} + G_m\mathbf{B}, \quad (\text{S-6})$$

and so the in-plane stresses are,

$$\sigma_{11} = \sigma_{22} = G_m(\lambda^2 - \frac{1}{\lambda^4}). \quad (\text{S-7})$$

Further, we derive the tension, T_b , from the first Piola-Kirchhoff stress,

$$T_b = G_m h (1 - \frac{1}{\lambda^6}). \quad (\text{S-8})$$

The static equilibrium shape of a membrane under a pressure loading is approximated by the Young-Laplace equation²,

$$\kappa + \frac{p}{T_b} = 0 \quad (\text{S-9})$$

Using the relation from Eg. S-4 and substituting the constitutive relations under biaxial loading conditions, we obtain a relation for the pressure as,

$$p \approx \frac{10G_m h}{D} (1 - \frac{1}{\lambda^6}) (\frac{\lambda}{\lambda_0} - 1)^{1/2}. \quad (\text{S-10})$$

S-III. MODEL PREDICTIONS OF SHEAR MODULUS

Fig. S-5 shows a comparison of the shear modulus, G , predicted independently using uniaxial and circular bulge tests. The predicted shear modulus is unchanged for different values of thickness (green data points) and pre-stretch (blue data points) tested.

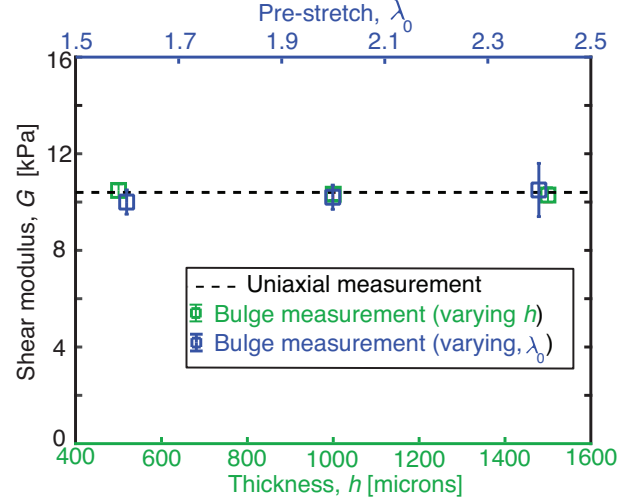


FIG. S-5. Depicts the comparison between shear modulus estimates obtained using uniaxial and bulge tests. The horizontal dashed line corresponds to the uniaxial test estimate. The green squares correspond to cases with varying thickness, whereas the blue squares depict the cases with different pre-stretches. Error bars represent the standard deviation of the data.

S-IV. SUPPLEMENTAL VIDEOS

Supplemental video S1: Unwrinkling of membrane [[link](#)]

Supplemental video S2: Biaxial Stretching device operation [[link](#)]

S-V. CAD FILES FOR STRETCHER FABRICATION

Part files for CAD assembly of biaxial stretcher. [[link](#)]

¹A. Gent, "A new constitutive relation for rubber," Rubber Chem. Technol. **69**, 59–61 (1996).

²R. M. Waldman and K. S. Breuer, "Camber and aerodynamic performance of compliant membrane wings," J. Fluid. Struct. **68**, 390–402 (2017).